Electro-chemo-mechanical effects of lithium incorporation in zirconium oxide

Jing Yang,[1] Mostafa Youssef,[1,*] and Bilge Yildiz[1,2,†]

[1]*Laboratory for Electrochemical Interfaces, Department of Materials Science and Engineering, Massachusetts Institute of Technology, 77 Massachusetts Avenue, Cambridge, Massachusetts 02139, USA*

[2]*Department of Nuclear Science and Engineering, Massachusetts Institute of Technology, 77 Massachusetts Avenue, Cambridge, Massachusetts 02139, USA*

(Received 10 March 2018; revised manuscript received 8 May 2018; published 26 July 2018)

Understanding the response of functional oxides to extrinsic ion insertion is important for technological applications including electrochemical energy storage and conversion, corrosion, and electronic materials in neuromorphic computing devices. Decoupling the complicated chemical and mechanical effects of ion insertion is difficult experimentally. In this work, we assessed the effect of lithium incorporation in zirconium oxide as a model system, by performing first-principles based calculations. The chemical effect of lithium is to change the equilibria of charged defects. Lithium exists in ZrO_2 as a positively charged interstitial defect, and raises the concentration of free electrons, negatively charged oxygen interstitials, and zirconium vacancies. As a result, oxygen diffusion becomes faster by five orders of magnitude, and the total electronic conduction increases by up to five orders of magnitude in the low oxygen partial pressure regime. In the context of Zr metal oxidation, this effect accelerates oxide growth kinetics. In the context of electronic materials, it has implications for resistance modulations via ion incorporation. The mechanical effect of lithium is in changing the volume and equilibrium phase of the oxide. Lithium interstitials together with zirconium vacancies shrink the volume of the oxide matrix, release the compressive stress that is needed for stabilizing the tetragonal phase ZrO_2 at low temperature, and promote tetragonal-to-monoclinic phase transformation. By identifying these factors, we are able to mechanistically interpret experimental results in the literature for zirconium alloy corrosion in different alkali-metal hydroxide solutions. These results provide a mechanistic and quantitative understanding of lithium-accelerated corrosion of zirconium alloy, as well as, and more broadly, show the importance of considering coupled electro-chemo-mechanical effects of cation insertion in functional oxides.

DOI: 10.1103/PhysRevMaterials.2.075405

I. INTRODUCTION

Ion insertion and extraction is a very common process in a number of technologically important applications, such as batteries [1,2], solid oxide fuel cells [3–5], ion transport membranes [6], electrochromic devices [7], and neuromorphic computing devices [8]. The response of the host material to extrinsic ions entering into its lattice is a complicated process, involving changes both in the chemical composition and in the stress state. Chemically, extrinsic doping changes the defect chemistry of the host material and thus influences ionic and electronic conduction. This is coupled to the mechanical response of the host material through chemical expansion/contraction [9]. Furthermore, changes in the defect concentration can alter the atomic structure and phase of the material, resulting in distinct electrical and magnetic properties as well as microstructure evolution [10–12]. Understanding the chemical and mechanical mechanisms in response to ion insertion and extraction is key to the design of better devices and materials. However, the complexity of such coupled processes makes it difficult, if not impossible, to separate contributions of individual factors experimentally and fully identify the underlying mechanisms.

In this work, we assess the coupled chemical and mechanical effects of lithium incorporation in ZrO_2 with density functional theory (DFT) calculations. ZrO_2 is chosen as the model material. It is the critical passivating layer in the corrosion of zirconium alloys used as fuel cladding in nuclear reactors [13]. It is also widely studied as high-k dielectrics in metal-oxide-semiconductor field-effect transistor (MOSFET) devices [14,15], as well as resistive switching devices [16,17]. Electrochemical control of Li content in CoO_2 has been shown as a utility for resistive processing [8], and it is feasible that Li can similarly tune the electronic conductivity of ZrO_2.

In light water reactors, zirconium alloys are used for cladding, enclosing the nuclear fuel. During operation, the tetragonal and monoclinic phases of the ZrO_2 passive layer grow on the outer layer of the cladding and protect the alloy from corrosion in high temperature coolant water. Lithium-accelerated corrosion is a well-known cladding corrosion phenomenon. In nuclear reactors, LiOH is added into the coolant water in contact with the cladding layer in order to balance the pH reduction caused by the boric acid that is added as a neutron absorber [18]. When zirconium alloy is immersed in aqueous solutions containing a high concentration of lithium ions, the oxide growth rate significantly increases

*Present address: Department of Mechanical Engineering, The American University in Cairo, AUC Avenue, P.O. Box 74, New Cairo 11835, Egypt.

†Corresponding author: byildiz@mit.edu

[19]. This phenomenon, called lithium-accelerated corrosion, is detrimental because lithium ions tend to concentrate locally at the oxide film surface [20]. The concentrated lithium ions further diffuse through the oxide film and result in localized accelerated corrosion [21]. Here we aim to resolve the mechanisms by which lithium insertion in ZrO_2 accelerates corrosion.

Our study revealed two distinct but coupled effects induced by lithium incorporation: (1) Lithium changes the defect chemistry of ZrO_2 and increases the concentration of zirconium vacancies, oxygen interstitials, and free electrons, and decreases that of free holes. The increase in oxygen interstitials leads to faster oxygen diffusion. The combined effect of increasing electron concentration and decreasing hole concentration leads to increase of total electronic conduction by up to five orders of magnitude in the low oxygen partial pressure regime. As a result, a net effect of accelerated oxide growth rate is expected. (2) Incorporation of lithium together with the accompanying zirconium vacancies increases the critical compressive stress that is needed for stabilizing the tetragonal ZrO_2 (T-ZrO_2). The T-ZrO_2 serves as a coherent protective layer against further oxidation and is only stabilized by the compressive stresses at the metal-oxide interface at the reactor operation temperatures (~300 °C) [22]. In the presence of lithium, the critical stress needed for stabilizing the T-ZrO_2 is much higher than the stress at the metal-oxide interface and so it transforms into the monoclinic phase (M-ZrO_2). This is a volume expansion process and should lead to cracks in the oxide film associated with accelerated corrosion. We validated our results with experimental reports of corrosion in the literature and helped explain the differences among corrosion effects of different alkali-metal hydroxide solutions.

II. METHODS

Density functional theory (DFT) calculations were performed with the Vienna *Ab Initio* Simulation Package (VASP) [23–26] using the generalized gradient approximation (GGA) with Perdew-Burke-Ernzerhof (PBE) functional [27,28]. The following are treated as valence electrons: $4s^2\,4p^6\,4d^2\,5s^2$ for zirconium, $2s^2 2p^4$ for oxygen, and $1s^2 2s^1$ for lithium. The chemical effect of lithium was assessed by comparing the equilibria of point defects with and without lithium in ZrO_2. Calculations related to defect formation energies were done on a supercell consisting of $2 \times 2 \times 2$ conventional unit cells of ZrO_2 with 700 eV energy cutoff and a $2 \times 2 \times 2$ k-point grid. The perfect cell was prerelaxed and we keep the volume and cell shape constant when relaxing the defect structures. The calculated defect formation energies were used to simulate the chemical effect of lithium in the dilute limit. Details of calculating the defect formation energies and equilibrium defect concentrations at different temperatures and oxygen partial pressures can be found in [29] for T-ZrO_2 and [30] for M-ZrO_2. In particular, the latter presents in detail how to model equilibrium defect chemistry with extrinsic aliovalent doping and we adopt that approach in this work. We consider zirconium oxide equilibrating with the environment of a fixed chemical potential of lithium, μ_{Li}.

To assess the mechanical effect induced by lithium ionic defects, we perform DFT calculations on several important defect species (1) by varying cell volume hydrostatically and allowing cell shape to change, and (2) by applying planar stress. The defective cells used here are all one defect in the 32-unit formula of ZrO_2. The resulting energy-volume (E-V) profile is fitted to the Birch-Murnaghan equation of state [31,32] to obtain the equilibrium volume V_0 and energy E_0.

$$E(V) = E_0 + \frac{9V_0B_0}{16}\left\{\left[\left(\frac{V_0}{V}\right)^{\frac{2}{3}} - 1\right]^3 B_0' + \left[\left(\frac{V_0}{V}\right)^{\frac{2}{3}} - 1\right]^2\left[6 - 4\left(\frac{V_0}{V}\right)^{\frac{2}{3}}\right]\right\}. \quad (1)$$

Here B_0 and B_0' represent the bulk modulus and its isothermal derivative with respect to pressure, respectively. The equilibrium volume acquired from the hydrostatic fixed volume calculations are compared to the volume of a perfect cell to obtain defect relaxation volumes.

Further, we evaluate the stress-volume (P-V) relationship predicted by the Birch-Murnaghan equation of state,

$$P(V) = \frac{3B_0}{2}\left[\left(\frac{V_0}{V}\right)^{\frac{7}{3}} - \left(\frac{V_0}{V}\right)^{\frac{5}{3}}\right] \times \left\{1 + \frac{3}{4}(B_0' - 4)\left[\left(\frac{V_0}{V}\right)^{\frac{2}{3}} - 1\right]\right\}, \quad (2)$$

which also gives the enthalpy-stress relationship by calculating $H = E + PV$. For biaxial stress, the energy change resulting from stress can be separated into a hydrostatic contribution and a deviatoric contribution. Here we extracted the hydrostatic part by fitting to the Birch-Murnaghan equation, which produces consistent pressure compared to the total stress calculated by DFT.

III. RESULTS AND DISCUSSION

In this section, we present the predicted chemical and mechanical effects of lithium incorporation in zirconium oxide of both the monoclinic and the tetragonal phase. We divide this section into three parts. First we present the defect chemistry of Li-doped ZrO_2 and how the Li doping changes electronic and oxygen transport in M-ZrO_2. Second, we look closely at the volume change induced by the dominant defect types in the presence of Li found in the first part, and the implication of those volume changes on the T-to-M phase transformation in ZrO_2. Last, we compare lithium with other alkali-metal elements to reveal its unique character regarding the coupled chemical and mechanical effect in ZrO_2.

A. Chemical effect of lithium insertion into ZrO_2

We consider various sites and valence states that lithium could take when incorporated into M-ZrO_2. For lithium sitting on a zirconium vacancy site, charge states from -5 to $+1$ were considered. For interstitial lithium, -1, 0 and $+1$ charge states are considered. DFT results show that the formation energies of all lithium substitutional defects have too high formation energy to have a significant concentration in the oxide matrix. For interstitial lithium, the dominating valence state is always

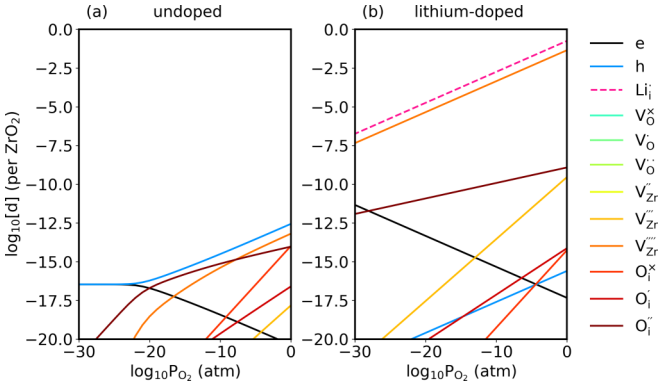

FIG. 1. Equilibrium defect concentrations predicted at 600 K for (a) undoped M-ZrO_2 and (b) Li-doped M-ZrO_2. Oxygen vacancies are not visible in the plotted range though they were explicitly calculated. Phonon vibrational free energies are included in calculating defect formation free energies as in Ref. [30].

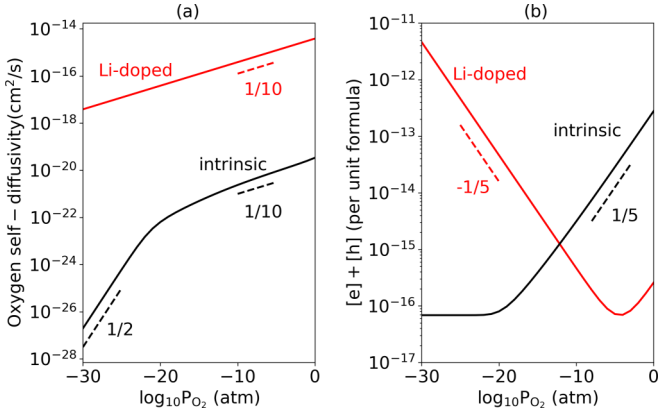

FIG. 2. (a) Oxygen self-diffusivity and (b) electron and hole concentration at 600 K for intrinsic M-ZrO_2 and Li-doped M-ZrO_2.

$Li_i^{\bullet}$. Detailed defect formation energy profiles can be found in the Supplemental Material (SM) [33], Sec. 1.

With the calculated formation energies, we obtained equilibrium concentrations of each defect following the method adopted in [29]. The computational framework captures defect energetics with first-principles calculations and feeds them to thermodynamic equilibria and charge neutrality calculations. This model predicts equilibrium defect concentrations as a function of temperature and oxygen partial pressure with no *a priori* assumption of dominant defect species. The defect concentrations in M-ZrO_2 as a function of oxygen partial pressure are shown in Fig. 1 at $T = 600$ K, which is close to the nuclear reactor operation temperature. The notation [defect] is used to represent concentration of the defect species per unit formula. Figure 1(a) shows the equilibria of intrinsic defects in M-ZrO_2. Throughout the oxygen partial pressure range, the holes are the dominant type of positively charged defect. The compensating species changes from being the free electron at low P_{O_2}, to O_i'' at intermediate P_{O_2}, and V_{Zr}'''' at high P_{O_2}. The situation changes when lithium is incorporated into the oxide matrix, as shown in Fig. 1(b) with $\mu_{Li} = -14.5$ eV. The chemical potential for lithium is referenced to that of lithium metal; i.e., for lithium metal $\mu_{Li} = 0$ eV. This choice of chemical potential corresponds a doping concentration of 10 ppm at intermediate P_{O_2}, consistent with experimentally reported Li concentration in the oxide layer on zirconium alloys [34]. We also examined a range of μ_{Li} which shows that the compensating mechanism does not change within the stability range. The results as a function of μ_{Li} can be found in SM, Sec. 2 [33].

Knowing that lithium exists the in ZrO_2 oxide matrix in the form of $Li_i^{\bullet}$, we can further analyze the change in native defect concentrations. The goal of examining defect chemistry upon lithium insertion is twofold. First, oxide growth rate is governed by oxygen diffusion and electronic conduction [18]. By knowing the oxygen-related defects, electrons, holes, and cation vacancies, we can understand the net effect of lithium insertion on the corrosion kinetics, here equivalent to the growth rate of the oxide. Second, it is also important to know how the dominant defects in the presence of $Li_i^{\bullet}$ alter the mechanical behavior of the oxide matrix. This is because mechanical stresses can lead to oxide film fracture, exposure of the metal to water, and accelerated corrosion. In the following, we present the major changes caused by Li on intrinsic defects related to these two aspects.

First, looking at oxygen-related defects, we find that O_i'' is the dominant oxygen defect species both before and after lithium insertion. Comparing Fig. 1(a) with Fig. 1(b), $[O_i'']$ is increased by about four orders of magnitude with lithium doping. This directly affects oxygen diffusivity, shown in Fig. 2(a). Here the total oxygen self-diffusivity D_{tot} is calculated with the random-walk model [35–37] by $D_{tot} = \sum_q [V_O^q] D_{V_O}^q + \sum_q [O_i^q] D_{O_i}^q$, where we use the diffusion coefficient of each defect type $D_{V_O}^q$ and $D_{O_i}^q$ from [38]. Derivations for the self-diffusivity expression in ionic solids can be found in Eqs. (3.6)–(3.9) in [35], or Eqs. (8.37) – (8.51) in [36]. At 600 K we see, in both the intrinsic and Li-doped M-ZrO_2, a $1/10 \log D_{tot}$-$\log P_{O_2}$ slope at the high P_{O_2} regime where V_{Zr}'''' is the dominant negatively charged defect. Because of the increase of oxygen interstitial concentration with lithium doping, D_{tot} rises also by about four orders of magnitude. At the low P_{O_2} regime this enhancement is even more profound. This is because the intrinsic M-ZrO_2 enters the hole-, compensation regime with a $1/2$ slope in $\log D_{tot}$-$\log P_{O_2}$, whereas the Li-doped M-ZrO_2 has a $1/10$ slope throughout the examined oxygen partial pressure range. At $P_{O_2} = 10^{-30}$ atm, we see a ten-orders-of-magnitude difference in D_{tot} comparing the two cases.

Next, for implications on electronic conduction, we take a close look at the change in electron and hole concentration. The dominant electronic carrier in the intrinsic M-ZrO_2 changes from being hole dominated at high P_{O_2} to $[e'] \approx [h^{\bullet}]$ at $P_{O_2} = 10^{-23}$ atm [Fig. 1(a)]. Upon lithium insertion, the hole concentration is greatly suppressed and electron concentration enhanced. The dominant electronic carrier type changes from being hole to electron at $P_{O_2} = 10^{-5}$ atm, and we no longer observe a regime where $[e'] \approx [h^{\bullet}]$. To show the net change in electronic conduction (assuming no change in mobilities), we plot $[e'] \approx [h^{\bullet}]$ in Fig. 2(b). In the hole-dominated region ($P_{O_2} > 10^{-5}$ atm), the total carrier concentration demonstrates a $1/5$ slope and decreases by three orders of magnitude upon lithium insertion. In the intermediate P_{O_2} range, the intrinsic

curve goes from hole dominated (1/5 slope) to $[e'] \approx [h^\bullet]$ (flat regime). Lithium-doped M-ZrO_2 transitions to the electron-dominated regime which exhibits a $-1/5$ slope in most of the P_{O_2} range. The relative change in electronic conduction changes sign at 10^{-11} atm; above this P_{O_2} lithium doping decreases electronic conduction while below it increases electronic conduction. The enhancement in electronic conduction becomes more and more significant with lowering of P_{O_2}. We observe a maximum of nearly five orders magnitude increase in the total carrier concentration at $P_{O_2} = 10^{-30}$ atm. This P_{O_2} is relevant both at the metal-oxide interface, and in the context of tuning effective P_{O_2} electrochemically, as has been demonstrated for other binary oxides [39–41].

Considering the above-described effects of Li both on oxygen defects and on electronic defects, a net acceleration of oxide growth is expected with lithium insertion. More specifically, comparing the effect of lithium on oxygen conduction versus electronic conduction, the change in the former (ten orders of magnitude at $P_{O_2} = 10^{-30}$ atm) is significantly larger than that in the latter (five orders of magnitude at $P_{O_2} = 10^{-30}$ atm). This is consistent with the dominant oxygen defects, O_i'', being -2 charged. Upon lithium insertion, electron chemical potential increases due to the n-type doping effect of lithium, lowering the formation energy of negatively charged defects. This lowering of formation energy is doubled for -2 charged oxygen interstitials compared to the -1 charged electrons. The effect on electronic conduction is reversed with varying P_{O_2}. In the context of zirconium alloy oxidation in water, the ZrO_2 layer is exposed to a gradient of oxygen partial pressure. The metal/oxide interface corresponds to the low P_{O_2} regime and the oxide/water interface corresponds to the high P_{O_2} regime. In M-ZrO_2 without Li, electronic conduction is more limited in the low P_{O_2} regime where electrons and holes compensate each other and the total conduction has no P_{O_2} dependence. With lithium doping, the electron becomes the dominant electronic carrier at low P_{O_2} and its concentration increases with decreasing P_{O_2}.

Besides the above-mentioned defects that are closely related to oxide growth rate, another important species is V_{Zr}'''', and it becomes the dominant charge compensating defect to lithium doping in the entire P_{O_2} range [Fig. 1(b)]. It is noteworthy that the increase in zirconium vacancy concentration must also result in an increase of zirconium diffusion, and thus, also accelerate the rate of oxide growth. However, the migration barrier of zirconium via the vacancy mechanism is much higher (7.18 eV [42]) compared to the migration barrier of oxygen interstitial (0.53 eV [38]). Even in the Li-doped case where $[V_{Zr}'''']$ is several orders of magnitude higher than $[O_i'']$, the contribution of cation diffusion to oxide growth should still be negligible compared to anion diffusion. However, as we shall see in the next section, increase of V_{Zr}'''' contributes greatly to the accelerated corrosion via its mechanical effect.

We provide the same analysis for T-ZrO_2 in SM, Sec. 3 [33]. Migration barriers for oxygen defects in T-ZrO_2 were used as provided in [37]. We conclude that the major defect chemistry response to lithium insertion is very similar in both phases, with $Li_i^\bullet$ and V_{Zr}'''' being the dominant compensating species, and all the conclusions made here also hold qualitatively for the tetragonal phase. We observe the suppression of oxygen interstitials and electrons in T-ZrO_2 on the same order of magnitude. The only difference is that the transition between electron versus hole domination as shown in Fig. 2 comes at a much lower P_{O_2} in T-ZrO_2, and therefore only the features at high P_{O_2} are observed.

B. Mechanical effect of lithium insertion into ZrO_2

Two types of mechanical responses of the oxide to extrinsic doping have been discussed in the literature and considered in this work. First, as we have seen in Sec. III A, extrinsic doping results in a significant change in defect chemistry. The resulting defect chemistry upon doping causes changes in the lattice parameter. This phenomenon is commonly observed in materials for energy conversion and storage, and often termed as chemical expansion [43]. Second, during the growth of the ZrO_2 passive film, T-to-M phase transformation results in volumetric dilation. The corresponding stress buildup cracks the film and leads to a porous microstructure [18]. Experimentally, it has been observed that lithium incorporation could change the relative fractions of T-ZrO_2 and M-ZrO_2 in the oxide film [21]. It is possible that lithium is behind the detrimental T-to-M phase transformation and the resulting changes in the film microstructure during oxide growth. In this section, we assess both types of mechanical responses.

We have concluded in Sec. III A that the major defect types in Li-doped ZrO_2 are $Li_i^\bullet$ and V_{Zr}'''' in both T-ZrO_2 and M-ZrO_2. First we assess the chemical expansion due to these dominant defects. We calculated the volume change introduced by these two types of defects. Figure 3 shows the DFT calculated energy with varying volume (colored dots). By fitting the results to the Birch-Murnaghan equation of state [Eq. (1), black dashed line], we can arrive at the equilibrium volume (vertical colored dashed line). The corresponding volume change for each defect is calculated by subtracting the volume of the perfect cell of the corresponding phase from the defective cell. In Ref. [44] it was suggested that this is a viable way to obtain the relaxation volume of charged defects in DFT supercells where the ambiguity of defining pressure in charged cells [45] is removed by fitting to an equation of state. We also note that

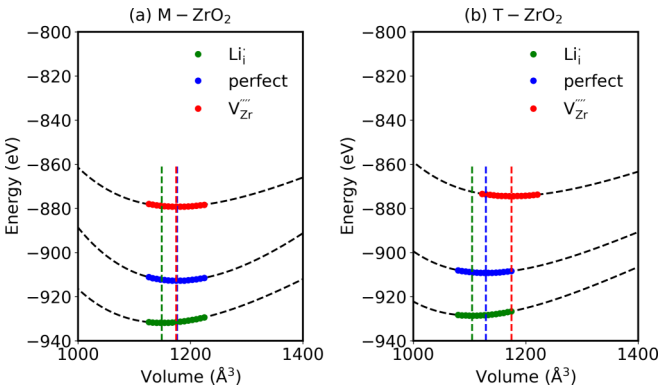

FIG. 3. Energy variation with volume for (a) M-ZrO_2 and (b) T-ZrO_2 calculated by DFT (colored dotted lines) and fitted by the Birch-Murnaghan equation of state (black dashed line). Equilibrium volumes predicted are shown by vertical dashed lines where minimum energy is reached.

TABLE I. Equilibrium volume per unit formula (in $Å^3$) for defect-free M-ZrO_2 and T-ZrO_2, one $Li_i^{\bullet}$ in 32 ZrO_2 and one V_{Zr}'''' in 32 ZrO_2. The fractional volume change is calculated with reference to perfect T-ZrO_2. The relaxation volume is defined by subtracting the volume of perfect cell from the defective cell of the same phase divided by 32.

	Perfect	$Li_i^{\bullet}$		V_{Zr}''''	
M-ZrO_2	Absolute volume ($Å^3$) 36.76 (+4.2%)	Absolute volume ($Å^3$) 35.91 (+1.8%)	Relaxation volume ($Å^3$) –0.85	Absolute volume ($Å^3$) 36.70 (+4.0%)	Relaxation volume ($Å^3$) –0.06
T-ZrO_2	Absolute volume ($Å^3$) 35.28 (0)	Absolute volume ($Å^3$) 34.52 (–2.2%)	Relaxation volume ($Å^3$) –0.77	Absolute volume ($Å^3$) 36.71(+4.0%)	Relaxation volume ($Å^3$) +1.42

the fractional volume change does not depend significantly on cell size, which is discussed in detail in SM, Sec. 4 [33]. The resulting equilibrium volumes are listed in Table I. In both the monoclinic and the tetragonal phase, the incorporation of lithium interstitial leads to volume shrinkage. To understand the contraction effect, in Fig. 4 we show the atomic structures of perfect M-/T-ZrO_2 and defective M-/T-ZrO_2 with $Li_i^{\bullet}$. We see that lithium interstitial resides within an oxygen cage and the O-O bonds of this cage shorten upon the insertion of lithium. This is because the positively charged $Li_i^{\bullet}$ effectively shares the electrons of surrounding oxygens and reduces their ionicity. As a result, the electrostatic repulsion between oxygen ions is suppressed and they are pulled closer towards each other.

On the other hand, the compensating species V_{Zr}'''' causes nearly no change of volume in M-ZrO_2 and a volume expansion in T-ZrO_2 (Fig. 3). Based on the defect equilibria we obtained in Sec. III A, each V_{Zr}'''' should be compensated by four $Li_i^{\bullet}$. In the dilute limit, the net effect of both defects is the sum of their relaxation volumes, which adds up to a 3.2% volume contraction in M-ZrO_2 and a 4.8% volume contraction in T-ZrO_2. The consequence of this contraction effect will be discussed in detail in Sec. III C.

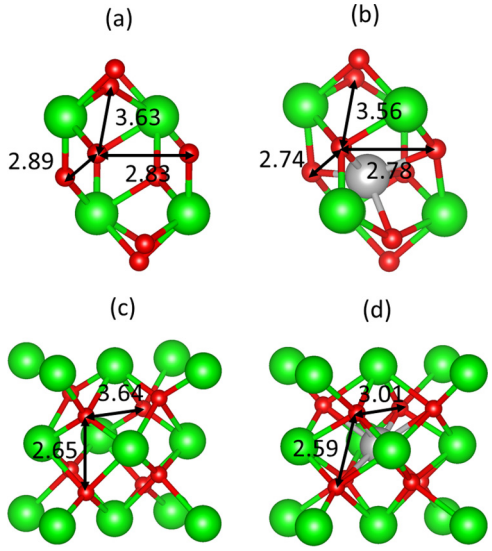

FIG. 4. Atomic structure of (a) perfect M-ZrO_2, (b) $Li_i^{\bullet}$ in M-ZrO_2, (c) perfect T-ZrO_2, and (d) $Li_i^{\bullet}$ in T-ZrO_2. Oxygen-oxygen bond lengths (in Å) within the oxygen cage that surrounds $Li_i^{\bullet}$ are marked on each graph. Green, red, and gray spheres represent zirconium, oxygen, and lithium ions, respectively.

In order to reveal the effect of lithium on T-to-M phase transformation, we further calculated the hydrostatic stress-enthalpy profile using the Birch-Murnaghan equation of state. In Fig. 5(a) we show the results for perfect T-ZrO_2 and M-ZrO_2. From the tensile stresses up to a compressive stress of $P = 10.51$ GPa (shown by vertical line), enthalpy of M-ZrO_2 H_M^{perfect} is smaller than that of T-ZrO_2 H_T^{perfect}. This is consistent with the fact that M-ZrO_2 is the stable phase at ambient pressure up to 1205 °C [46]. At $P = 10.51$ GPa ΔH crosses zero and we enter the regime where T-ZrO_2 is stabilized by compressive stress. Experimentally, critical compressive stress of T-to-M phase transformation was measured to be 6 GPa [47,48]. Our theoretical prediction is in reasonable agreement with the measured value.

We assessed the effect of defects on the T-to-M phase transformation by calculating how they change this critical compressive stress. In Fig. 5(b) the H-P result for a $2 \times 2 \times 2$ ZrO_2 cell containing one $Li_i^{\bullet}$ is shown. The transition stress is slightly increased to 11.11 GPa compared to the perfect cell case, which is seemingly a minor effect. Next we take into consideration the increase of zirconium vacancies, V_{Zr}'''', in the presence of lithium insertion [Fig. 5(c)]. The calculated effect of those defects is to increase substantially the critical stress needed to stabilize the T-ZrO_2. In the stress range examined directly by DFT calculations, −10 to 20 GPa, there exists no stress that stabilizes T-ZrO_2. When we extrapolate the data range by using the Birch-Murnaghan equation of state, we find that the T-ZrO_2 phase can be stabilized at substantially larger compressive stresses, nearly 60 GPa and above.

The situation remains qualitatively similar when we switch to the planar stress scenario, as shown in Figs. 5(d)–5(f). The predicted compressive planar stress to stabilize T-ZrO_2 is at or above 12 GPa for the defect free case [Fig. 5(d)], and almost does not change with the addition of one $Li_i^{\bullet}$ in the 32-unit formula of ZrO_2 [Fig. 5(e), 11.79 GPa]. The transition stress rises about 20% (from 11.97 to 14.13 GPa) with V_{Zr}'''', which is a significant effect in promoting the T-to-M phase transformation in ZrO_2.

These results have direct implications to explaining the cyclic kinetics of corrosion on zirconium alloys [13]. During the oxidation process, initially the tetragonal phase ZrO_2 is stabilized by interfacial compressive stress. The formed, well-textured T-ZrO_2 layer slows down oxygen incorporation and the oxide film thickness plateaus. However, the T-to-M phase transformation induced by stress release drives the formation of cracks and pores. Interconnected cracks and pores serve as a fast path for diffusing species and results in acceleration of the corrosion kinetics [49]. Here our results clearly demonstrate

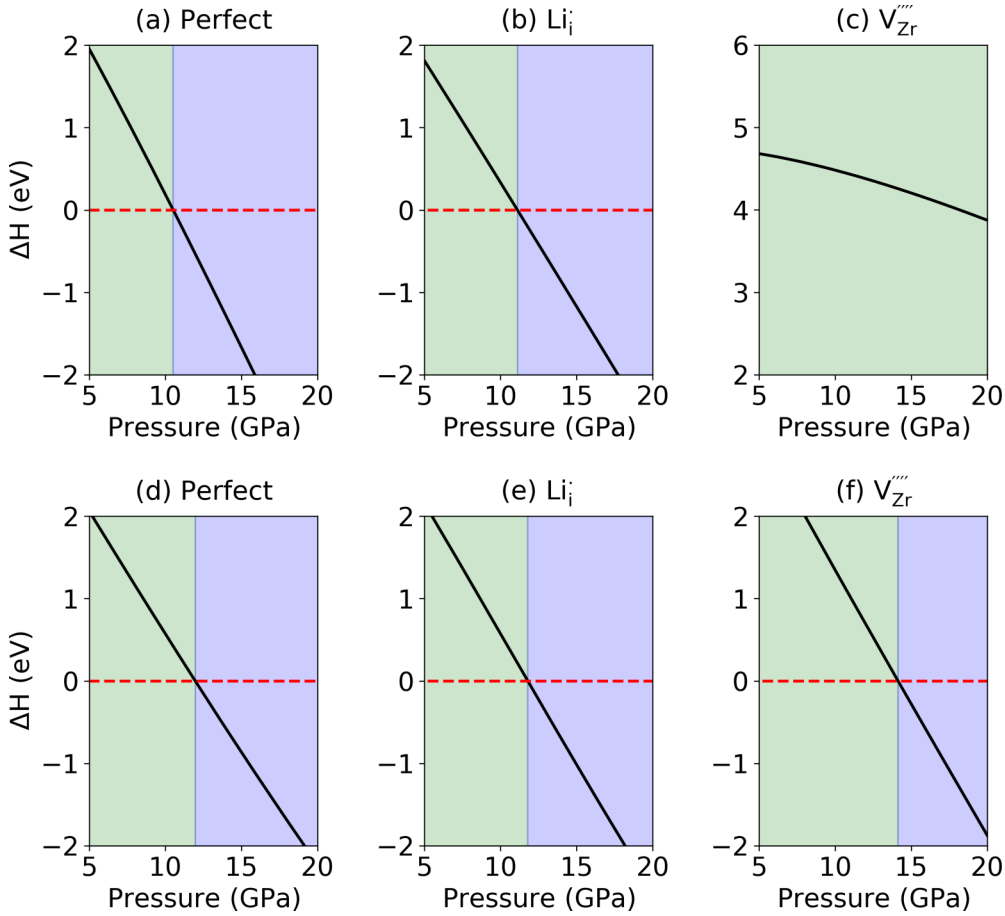

FIG. 5. Enthalpy difference, ΔH, between the tetragonal and the monoclinic phases of ZrO_2, calculated by fixed volume hydrostatic stress in (a–c), and planar stress in (d–f). Here ΔH presents the enthalpy of the monoclinic phase subtracted from the enthalpy of the tetragonal phase. The tetragonal phase is stabilized in the pressure range where $\Delta H < 0$ (represented by blue) and monoclinic phase is stabilized where $\Delta H > 0$ (represented by green). The cell configurations are (a,d) perfect with no defect, (b,e) with one singly charged lithium interstitial $Li_i^{\bullet}$, and (c,f) with one quadruply charged zirconium vacancy $V_{Zr}^{''''}$. The boundaries between blue and green regions show the stress at which ΔH crosses zero, i.e., the critical stress where T-to-M phase transformation happens.

that lithium incorporation releases the compressive stress, destabilizes the T-ZrO_2, and promotes the volume-expansive T-to-M phase transformation. As a result, lithium incorporation accelerates the transition from passive to the accelerated breakaway corrosion process. In the next section we provide a detailed comparison between this prediction and experimental observations.

C. Comparing the relative importance of the chemical and mechanical effects of Li insertion in ZrO_2

In the previous two sections, we have concluded that (1) chemically, lithium works as a donor dopant in ZrO_2. The lithium dopant resides dominantly in the form of $Li_i^{\bullet}$. O_i'' concentration is enhanced and leads to faster oxygen diffusion. Electron concentration is increased and holes decreased, leading to a net effect of electronic conduction increase in the low P_{O_2} n-type regime. $V_{Zr}^{''''}$ becomes the dominant negatively charged defect species compensating the positively charged lithium interstitial in the entire P_{O_2} range considered. (2) Mechanically, lithium incorporation, together with the increased $V_{Zr}^{''''}$ concentration, increases the compressive stress that is needed to stabilize the T-ZrO_2 and thus promotes the T-to-M phase transformation in the growing oxide layer. In this part, we resolve the conditions under which the chemical effect or the mechanical effect dominates behind the lithium-accelerated corrosion of zirconium alloys.

In order to do this, we compare the influence of other alkali-metal elements with lithium. Chemically, alkali-metal elements should behave similarly, but mechanically they can be very different because of the increasing ionic radius going down along one column in the periodic table. Jeong *et al.* conducted experiments of zirconium alloy corrosion in aqueous alkali hydroxide solutions (LiOH, NaOH, KOH, RbOH, and CsOH) [50]. They found that with relatively low concentration of the alkali element in solution (4.3 mM), the oxide film growth behaves similarly in all alkali hydroxide solutions with a modest acceleration effect arising from each. The order of the acceleration intensity is strongest for LiOH, and less and less intense going down the periodic table column. On the other hand, in the high concentration regime (32.5 mM), oxidation film growth kinetics in LiOH solution is very different from all other alkali-metal elements, with a significantly higher growth rate compared to the corrosion rate in NaOH, KOH,

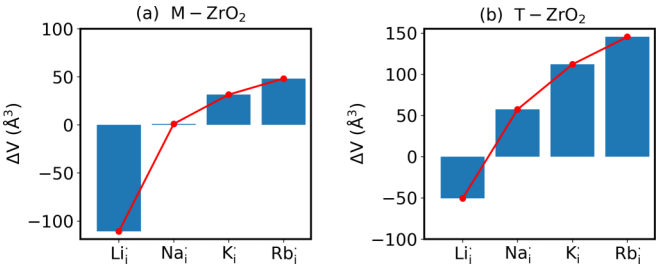

FIG. 6. Volume change induced by alkali-metal element incorporation into (a) monoclinic phase ZrO_2 and (b) tetragonal phase ZrO_2, considering the four singly charged alkali-metal interstitials $M_i^{\bullet}$ compensated by one quadruply charged zirconium vacancy V_{Zr}''''.

RbOH, and CsOH. The weight gain in LiOH solution is over 2500 mg/dm^2 after 300 days, but lower than 200 mg/dm^2 in all other alkali-metal solutions.

The observed difference between alkali-metal solutions can be well explained by considering both the chemical and mechanical effects. In the low concentration regime, enhancement in oxygen diffusivity and electronic conductivity (chemical effect) with alkali-metal element incorporation dominates in the acceleration effect. Since all the alkali-metal elements act as interstitial donors and promote the concentration of negatively charged defect species (oxygen interstitial in particular), they all have a modest and comparable influence on the oxide growth rate. The easiness of the alkali-metal element entering the ZrO_2 film should depend on its ionic radius. The ionic radius of Zr^{4+} is 72 pm, and the ionic radii for Li^+, Na^+, K^+, Rb^+, and Cs^+ are 76, 102, 151, 161, and 174 pm, respectively [51]. From this comparison, being the smallest it should be easiest for Li^+ to get incorporated in the oxide film as an interstitial defect. That is, the doping concentration of lithium as a function of time should be the highest compared to other alkali metals entering the oxide from the hydroxide solutions. As a result, the enhancement of oxygen diffusivity and electronic conductivity is most significant with LiOH, and gradually weakens down the periodic table column.

In the high concentration regime, the sharp increase of corrosion rate in LiOH is most likely related to change in microstructure (mechanical effect) of the oxide film. We have shown in the previous section that lithium incorporation introduces two effects related to phase transformation of ZrO_2. First, $Li_i^{\bullet}$ leads to volume shrinkage and releases the compressive stress needed for stabilizing the protective tetragonal phase ZrO_2. Second, $Li_i^{\bullet}$ promotes the concentration of V_{Zr}'''' which increases the compressive stress needed for stabilizing T-ZrO_2. Under expected compressive stresses at the metal-oxide interface, which is reported to be 4–6 GPa with 50-nm-thick oxide film [47], the T-ZrO_2 should transform to M-ZrO_2 when lithium enters the oxide. The induced expansive phase transformation leads to cracks, pores, and open grain boundaries in the oxide film and further increases oxidation rate.

Now we ask the question of why this microstructure effect is only seen in LiOH, but not in other alkali hydroxide solutions. In Fig. 6 we show the total relaxation volume of the compensating pair V_{Zr}'''' and four $M_i^{\bullet}$, where M stands for the alkali-metal element. The volume change of individual defect is calculated using the same approach as described in the previous section, with one defect in the 32-unit formula of ZrO_2. It is clear that in both T-ZrO_2 and M-ZrO_2, lithium is the only alkali-metal element that leads to a volume shrinkage. All other alkali-metal elements lead to volume expansion. In all cases, the effect of V_{Zr}'''' increasing the critical pressure for phase transformation exists. However, for Na, K, and Rb, chemical expansion increases the compressive stress in the oxide film, and enables the retaining of the T phase of ZrO_2, that is, the more protective phase forming coherently at the metal-oxide interface under compressive stress. As a result, we do not observe significant microstructure variation in any alkali hydroxide solutions except for LiOH. This provides the basis of explanation of the above-mentioned experimental observation.

IV. CONCLUSION

In this paper we assessed the coupled chemical and mechanical effects of lithium incorporation in ZrO_2, and how these effects can contribute to accelerated oxidative corrosion of Zr. We have discovered two major mechanisms: (1) Based on the dilute-limit defect chemistry equilibria, lithium acts as a donor in ZrO_2 in the form of $Li_i^{\bullet}$. Upon insertion, $[O_i'']$ is increased by up to ten orders of magnitude, leading to faster oxygen diffusion. Electron concentration is increased by up to five orders of magnitude, and hole concentration is decreased by three orders of magnitude. The net electronic conduction is increased in the low P_{O_2} n-type regime. An overall outcome of these two chemical effects should be faster oxide growth rate. At the same time, V_{Zr}'''' is greatly enhanced in the entire P_{O_2} range. (2) Based on the mechanical response, lithium incorporation and subsequent increase in V_{Zr}'''' increases the compressive stress that is needed to stabilize T-ZrO_2, and this promotes the detrimental T-to-M phase transformation and cracks in the oxide film. By comparing the distinct behavior of LiOH compared to other alkali-metal hydroxide solutions, we have identified the first effect being dominant in the low alkali-metal concentration regime, and the second effect being dominant in the high concentration regime. We believe that this work shows the importance of examining the response of charged defects to alkali-metal ion insertion in the metal oxide, and the coupling of that chemical effect to the mechanical response, for better understanding complex and coupled processes taking place in metal oxidation in alkali hydroxide solutions. The results have implications for understanding the electronic and mechanical properties of ZrO_2 in energy conversion, storage, and information processing applications as well.

ACKNOWLEDGMENTS

This work is supported by the Consortium for Advanced Simulation of Light Water Reactors (CASL), an Energy Innovation Hub for Modeling and Simulation of Nuclear Reactors under US Department of Energy Contract No. DE-AC05-00OR22725. We acknowledge the Extreme Science and Engineering Discovery Environment (XSEDE) program for calculations performed under Allocation No. TG-DMR120025.

[1] M. Broussely, P. Biensan, and B. Simon, Electrochim. Acta **45**, 3 (1999).

[2] D. Kundu, E. Talaie, V. Duffort, and L. F. Nazar, Angew. Chem., Int. Ed. **54**, 3431 (2015).

[3] E. D. Wachsman and K. T. Lee, Science **334**, 935 (2011).

[4] A. Chroneos, B. Yildiz, A. Tarancón, D. Parfitt, and J. A. Kilner, Energy Environ. Sci. **4**, 2774 (2011).

[5] E. D. Wachsman, C. A. Marlowe, and K. T. Lee, Energy Environ. Sci. **5**, 5498 (2012).

[6] P. N. Dyer, R. E. Richards, S. L. Russek, and D. M. Taylor, Solid State Ionics **134**, 21 (2000).

[7] D. T. Gillaspie, R. C. Tenent, and A. C. Dillon, J. Mater. Chem. **20**, 9585 (2010).

[8] E. J. Fuller, F. E. Gabaly, F. Léonard, S. Agarwal, S. J. Plimpton, R. B. Jacobs-Gedrim, C. D. James, M. J. Marinella, and A. A. Talin, Adv. Mater. **29**, 1604310 (2017).

[9] D. Marrocchelli, S. R. Bishop, H. L. Tuller, and B. Yildiz, Adv. Funct. Mater. **22**, 1958 (2012).

[10] M. V. Patrakeev, J. A. Bahteeva, E. B. Mitberg, I. A. Leonidov, V. L. Kozhevnikov, and K. R. Poeppelmeier, J. Solid State Chem. **172**, 219 (2003).

[11] E. Enriquez, A. Chen, Z. Harrell, P. Dowden, N. Koskelo, J. Roback, M. Janoschek, C. Chen, and Q. Jia, Sci. Rep. **7**, 46184 (2017).

[12] Q. Lu and B. Yildiz, Nano Lett. **16**, 1186 (2016).

[13] A. T. Motta, A. Couet, and R. J. Comstock, Annu. Rev. Mater. Res. **45**, 311 (2015).

[14] A. I. Kingon, J.-P. Maria, and S. K. Streiffer, Nature **406**, 1032 (2000).

[15] M. Copel, M. Gribelyuk, and E. Gusev, Appl. Phys. Lett. **76**, 436 (2000).

[16] C. Y. Lin, C. Y. Wu, C. Y. Wu, T. C. Lee, F. L. Yang, C. Hu, and T. Y. Tseng, IEEE Electron Device Lett. **28**, 366 (2007).

[17] R. Huang, X. Yan, S. Ye, R. Kashtiban, R. Beanland, K. A. Morgan, M. D. B. Charlton, and C. H. de Groot, Nanoscale Res. Lett. **12**, 384 (2017).

[18] B. Cox, J. Nucl. Mater. **336**, 331 (2005).

[19] S. Müller and L. Lanzani, J. Nucl. Mater. **439**, 251 (2013).

[20] J. Deshon, D. Hussey, B. Kendrick, J. McGurk, J. Secker, and M. Short, JOM **63**, 64 (2011).

[21] W. Liu, B. Zhou, Q. Li, and M. Yao, Corros. Sci. **47**, 1855 (2005).

[22] P. Wang and G. S. Was, J. Mater. Res. **30**, 1335 (2015).

[23] G. Kresse and J. Hafner, Phys. Rev. B **47**, 558 (1993).

[24] G. Kresse and J. Hafner, Phys. Rev. B **49**, 14251 (1994).

[25] G. Kresse and J. Furthmüller, Comput. Mater. Sci. **6**, 15 (1996).

[26] G. Kresse and J. Furthmüller, Phys. Rev. B **54**, 11169 (1996).

[27] J. P. Perdew, K. Burke, and M. Ernzerhof, Phys. Rev. Lett. **77**, 3865 (1996).

[28] J. P. Perdew, K. Burke, and M. Ernzerhof, Phys. Rev. Lett. **78**, 1396 (1997).

[29] M. Youssef and B. Yildiz, Phys. Rev. B **86**, 144109 (2012).

[30] M. Youssef, M. Yang, and B. Yildiz, Phys. Rev. Appl. **5**, 014008 (2016).

[31] F. D. Murnaghan, Proc. Natl. Acad. Sci. U.S.A. **30**, 244 (1944).

[32] F. Birch, Phys. Rev. **71**, 809 (1947).

[33] See Supplemental Material at http://link.aps.org/supplemental/10.1103/PhysRevMaterials.2.075405 for additional details on calculations with lithium defects and their effects in T-ZrO_2.

[34] A. Krausová, J. Macák, P. Sajdl, R. Novotný, V. Renčiuková, and V. Vrtílková, J. Nucl. Mater. **467**, 302 (2015).

[35] Y.-M. Chiang, D. P. Birnie, and W. D. Kingery, *Physical Ceramics: Principles for Ceramic Science and Engineering* (Wiley, New York, 1996).

[36] R. W. Balluffi, S. Allen, and W. C. Carter, *Kinetics of Materials* (John Wiley & Sons, New York, 2005).

[37] M. Youssef and B. Yildiz, Phys. Rev. B **89**, 024105 (2014).

[38] J. Yang, M. Youssef, and B. Yildiz, Phys. Rev. B **97**, 024114 (2018).

[39] W. C. Chueh, A. H. McDaniel, M. E. Grass, Y. Hao, N. Jabeen, Z. Liu, S. M. Haile, K. F. McCarty, H. Bluhm, and F. E. Gabaly, Chem. Mater. **24**, 1876 (2012).

[40] D. Chen, S. R. Bishop, and H. L. Tuller, Chem. Mater. **26**, 6622 (2014).

[41] M. T. Greiner, L. Chai, M. G. Helander, W.-M. Tang, and Z.-H. Lu, Adv. Funct. Mater. **23**, 215 (2013).

[42] L. B. Shi, Y. P. Wang, and M. B. Li, Mater. Sci. Semicond. Process. **27**, 586 (2014).

[43] S. R. Bishop, D. Marrocchelli, C. Chatzichristodoulou, N. H. Perry, M. B. Mogensen, H. L. Tuller, and E. D. Wachsman, Annu. Rev. Mater. Res. **44**, 205 (2014).

[44] M. Youssef, B. Yildiz, and K. J. Van Vliet, Phys. Rev. B **95**, 161110 (2017).

[45] F. Bruneval, C. Varvenne, J.-P. Crocombette, and E. Clouet, Phys. Rev. B **91**, 024107 (2015).

[46] J. P. Abriata, J. Garcés, and R. Versaci, Bull. Alloy Phase Diagrams **7**, 116 (1986).

[47] Y.-S. Kim, Y.-H. Jeong, and J.-N. Jang, J. Nucl. Mater. **412**, 217 (2011).

[48] M. Guerain, C. Duriez, J. L. Grosseau-Poussard, and M. Mermoux, Corros. Sci. **95**, 11 (2015).

[49] A. Garner, A. Gholinia, P. Frankel, M. Gass, I. MacLaren, and M. Preuss, Acta Mater. **80**, 159 (2014).

[50] Y. H. Jeong, J. H. Baek, S. J. Kim, H. G. Kim, and H. Ruhmann, J. Nucl. Mater. **270**, 322 (1999).

[51] R. D. Shannon, Acta Crystallogr., Sect. A: Cryst. Phys., Diffr., Theor. Gen. Crystallogr. **32**, 751 (1976).